





Observation of antiferromagnetic domains in Cr_2O_3 using nonreciprocal optical effects

T. Hayashida , K. Arakawa, T. Oshima , K. Kimura , and T. Kimura 

Department of Advanced Materials Science, University of Tokyo, Kashiwa, Chiba 277–8561, Japan



(Received 27 July 2022; accepted 30 September 2022; published 27 October 2022)

The archetypal magnetoelectric (ME) antiferromagnet Cr_2O_3 , which has the diagonal components of linear ME tensor, exhibits several different types of nonreciprocal optical effects: the electric field-induced (E -induced) Faraday effect, the electric field-induced magnetic circular dichroism (E -induced MCD), and the spontaneous nonreciprocal rotation of reflected light (NRR). In principle, antiferromagnetic (AFM) domains of Cr_2O_3 are expected to be distinguished by using these effects. However, such domain observations have never been reported mainly due to the smallness of the effects studied to date. In this study, we demonstrate that all these nonreciprocal optical effects allow the observation of AFM domains in Cr_2O_3 . We first measured spectra of the E -induced Faraday effect and E -induced MCD, and found that relatively large effects appear in the visible light region. Then, by imaging spatial distributions of the three nonreciprocal effects via field and light-polarization modulation imaging techniques, we succeeded in visualizing AFM domains. Intriguingly, the domain patterns obtained via the bulk sensitive E -induced Faraday effect and MCD and those via the surface-sensitive NRR are identical to each other, revealing that the AFM domains in Cr_2O_3 are uniform in the thickness direction. The domain observation methods provided here will be widely applied to various ME antiferromagnets, not only insulators but also metals, with the diagonal components of linear ME tensor.

DOI: [10.1103/PhysRevResearch.4.043063](https://doi.org/10.1103/PhysRevResearch.4.043063)

I. INTRODUCTION

Materials with broken time-reversal symmetry exhibit nonreciprocal optical effects, represented by the Faraday and magneto-optical Kerr effects owing to net magnetization. In addition to such conventional effects, unconventional nonreciprocal optical effects occur when space-inversion symmetry is also broken in such materials. This is due to the presence of a linear magnetoelectric (ME) coupling in which electric polarization P (magnetization M) is linearly induced by a magnetic field H (an electric field E), described as $P_i = \alpha_{ij}H_j$ ($\mu_0M_i = \alpha_{ij}E_j$). Here, α_{ij} is linear ME tensor where i and j run over all the Cartesian coordinates and μ_0 is permeability of vacuum. A representative unconventional nonreciprocal effect is nonreciprocal directional dichroism (NDD), that is, asymmetry in absorption between two counterpropagating light beams. It originates from the off-diagonal components of α_{ij} ($i \neq j$) expanded to optical frequencies and has been widely studied in various materials and in various frequency bands [1–9]. Furthermore, NDD in the visible to near-infrared regions has been applied to distinguish and visualize domain states in fully compensated antiferromagnetic (AFM) materials [10–13].

The diagonal components of α_{ij} ($i = j$) also contributes to unconventional nonreciprocal optical effects. In this paper,

we focus on the following three effects. The first one is the electric field-induced (E -induced) Faraday effect [14–19]. As its name suggests, it refers to the polarization rotation of transmitted light induced by applying an electric field. Though there are linear and quadratic E -induced Faraday effects [15], we refer to the former one as E -induced Faraday effect in this paper. ME materials with the diagonal components of α_{ij} (diagonal ME materials) exhibit the E -induced Faraday effect when an electric field is applied (anti)parallel to light propagation direction. This effect is intuitively understood considering that a magnetization is induced in the same direction with an applied electric field. However, an antiferromagnetic order parameter also contributes to this effect as discussed in the following sections. In addition, like the magnetic circular dichroism, which is a counterpart of the Faraday effect related by the Kramers-Kronig relation, diagonal ME materials will also exhibit the electric field-induced magnetic circular dichroism (E -induced MCD).

Another unconventional nonreciprocal optical effect is the nonreciprocal rotation of reflected light (NRR) [20–22]. Although NRR is similar to the magneto-optical Kerr effect [23,24], it is not ascribed to net magnetization. Instead, NRR derives from the diagonal components of α_{ij} expanded to optical frequencies, as described in detail in the following section. Note that diagonal ME materials also exhibit another nonreciprocal optical effect in the transmittance setting, so-called gyrotropic birefringence (GB) [20,25–28] though we do not treat it in this paper.

In contrast to the widely studied NDD owing to the off-diagonal components of α_{ij} , the above-mentioned nonreciprocal optical effects owing to the diagonal components of α_{ij} have been less investigated. Especially, E -induced Faraday

Published by the American Physical Society under the terms of the [Creative Commons Attribution 4.0 International license](https://creativecommons.org/licenses/by/4.0/). Further distribution of this work must maintain attribution to the author(s) and the published article's title, journal citation, and DOI.

effect, NRR, and GB in the visible to near-infrared regions are expected to be useful to distinguish AFM domain states [17,21], but the visualization of AFM domains by using these effects has not been reported. It is most likely because these effects are known to be relatively small.

Here, we study the above-mentioned unconventional nonreciprocal optical effects in the archetypical ME material Cr_2O_3 to overcome the difficulty in visualizing AFM domains via the diagonal ME effect. First, by measuring spectra of the E -induced Faraday effect and E -induced MCD in the visible light region, we show that Cr_2O_3 exhibits relatively large effects at wavelengths around the spin-allowed $d-d$ transitions. Second, we visualize AFM domains of Cr_2O_3 using the E -induced Faraday effect, E -induced MCD, and NRR. This success is achieved by adopting the electric-field modulation imaging and the polarization modulation imaging, both of which are effective to resolve spatial distributions of small signals.

This paper is organized as follows: In Sec. II, we introduce the target material Cr_2O_3 and its unconventional nonreciprocal optical effects: E -induced Faraday effect, E -induced MCD, and NRR. In Sec. III, experimental methods about sample preparation and measurements of the unconventional nonreciprocal optical effects are introduced. In Sec. IV, we show the results and discuss them. Finally in Sec. V, we summarize our work.

II. NONRECIPROCAL OPTICAL EFFECTS IN Cr_2O_3

Cr_2O_3 is the material in which the ME effect was predicted and observed for the first time [29,30]. The crystal structure of Cr_2O_3 is described by the corundum structure (space group $R\bar{3}c$). At temperatures (T) below $T_N \approx 307$ K, it shows an AFM ordering [31,32]. The magnetic symmetry in the AFM phase is $\bar{3}'m'$, which allows the diagonal ME effects with nonzero ME tensor components of $\alpha_{11} = \alpha_{22}$ and α_{33} [33]. A pair of domain states ($L+$ and $L-$), which is related by either time reversal or space inversion, develops in the AFM phase [Fig. 1(a)]. So far, such domain states have been visualized by using second-harmonic generation [34], magnetoelectric force microscopy [35], x-ray magnetic circular dichroism [36,37], and nanoscale scanning diamond magnetometry [38–40].

A. E -induced Faraday effect and E -induced MCD

Cr_2O_3 will show the E -induced Faraday effect and E -induced MCD in any direction if an applied electric field (\mathbf{E}) and light propagation direction (\mathbf{k}) are (anti)parallel to each other. So far, the E -induced Faraday effect in Cr_2O_3 has been measured at several wavelengths [14–18], but its spectrum has not been provided. Experimentally, to avoid the contribution of birefringence, it is convenient to adopt the experimental setting in which both \mathbf{E} and \mathbf{k} are along the hexagonal c axis. Thus, the E -induced effects in this setting ($\mathbf{E} \parallel \mathbf{k} \parallel c$) are discussed below.

The E -induced Faraday effect is described by the polarization rotation ϕ [deg] induced in proportion to an applied electric field as

$$\phi = \beta \times E_c \times d = \beta V_c, \quad (1)$$

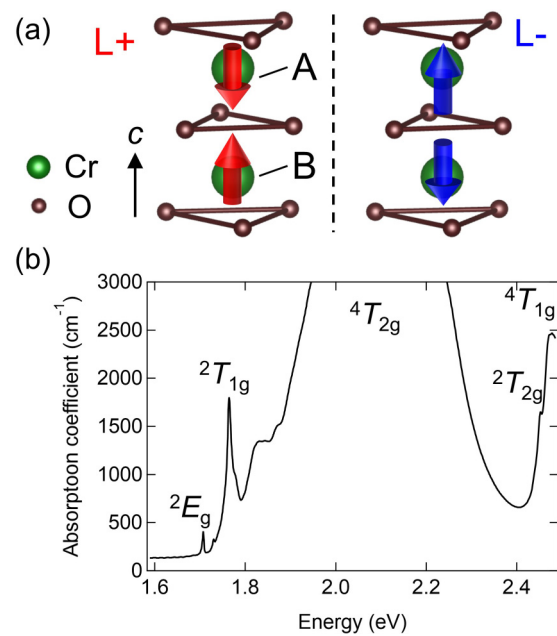


FIG. 1. Magnetoelectric antiferromagnet Cr_2O_3 . (a) Antiferromagnetic domains of Cr_2O_3 . The red and blue arrows represent Cr spins. Here, the two Cr sites denoted as A and B, which characterize the two domain states of $L+$ and $L-$, are depicted. (b) Absorption spectrum obtained at 83 K in geometry of $\mathbf{k} \parallel c$ in the photon energy range of $1.58 \text{ eV} < E_{\text{ph}} < 2.48 \text{ eV}$. The labels 2E_g , ${}^2T_{1g}$, ${}^4T_{2g}$, ${}^2T_{2g}$, and ${}^4T_{1g}$ are the irreducible representations of the excited states corresponding to the absorption peaks.

where β [deg V^{-1}] is the coefficient representing the magnitude of the E -induced Faraday effect, E_c [V cm^{-1}] = $V_c[\text{V}]/d[\text{cm}]$ is an applied electric field along the c axis, V_c [V] is an applied voltage, and d [cm] is a sample thickness. In the same manner, the E -induced MCD is defined as a difference in an absorption coefficient for right (α_R) and left (α_L) circularly polarized light ($\alpha_{\text{MCD}} = \alpha_R - \alpha_L$ [cm^{-1}]) induced in proportion to an applied electric field and described as

$$\alpha_{\text{MCD}} = (\alpha_0 - \beta' E_c) - (\alpha_0 + \beta' E_c) = -2\beta' E_c, \quad (2)$$

where β' [V^{-1}] is the coefficient representing the magnitude of E -induced MCD and α_0 is an absorption coefficient for right and left circularly polarized light in zero electric field. So far, the E -induced Faraday effect has been measured at some wavelengths in the near-infrared region and at 632.8 nm (e.g., $\beta \approx 10^{-5} \sim 10^{-6} \text{ deg V}^{-1}$) [14–17].

According to a previous study, the E -induced Faraday effect (and related E -induced MCD) in Cr_2O_3 is characterized by two contributions [16,17]. One is the term proportional to the ME coefficient α_{33} , and the other is the term proportional to the AFM order parameter l . Here, l is defined as the difference of the magnetic moments at site A and site B with opposite spins [see Fig. 1(a)], i.e., $l = m_A - m_B$ [16,17]. When an electric field is applied, not only net magnetization $\alpha_{33} E_c$ is induced but also the Cr^{3+} ions at sites A and B are slightly displaced along the c axis in opposite directions. This shift makes the crystal field around the Cr^{3+} ions at site A and site B distinct from each other, which causes the E -induced

Faraday effect and related E -induced MCD proportional to l . In short, the coefficients β and β' are described as

$$\beta = p\alpha_{33} + ql, \quad (3)$$

$$\beta' = p'\alpha_{33} + q'l, \quad (4)$$

where $p(p')$ and $q(q')$ are the contribution coefficients from α_{33} and l to the E -induced Faraday effect (E -induced MCD), respectively. The contribution ratio of p/q depends on the frequency of incident light, and such frequency dependence was discussed based on the T dependence of β in Ref. [17]. We will discuss the microscopical origins of β and β' in Sec. IV. Importantly, because the signs of α_{33} and l get reversed when the domain states ($L+$ and $L-$) are flipped, the signs of β and β' depend on the domain states. Thus, the domain structures of Cr_2O_3 can be distinguished by using these effects.

B. NRR

Rotation θ and ellipticity ε of reflected light in geometry $\mathbf{k} \parallel c$ are given by [20,22]

$$\theta + i\varepsilon = 2\alpha_{\perp} \frac{1 + n_{\perp}}{1 - n_{\perp}}, \quad (5)$$

where $\alpha_{\perp} = \alpha_{11}(\omega) = \alpha_{22}(\omega)$ is the ME coefficients expanded to the optical frequencies and $n_{\perp}^2 = \epsilon_{11}(\omega) = \epsilon_{22}(\omega)$ is the dielectric constant. Here, the sign of α_{\perp} depends on the domain states of $L+$ and $L-$, and thus NRR is also useful to distinguish AFM domains of Cr_2O_3 . The NRR spectra in the visible light region were observed in Ref. [22], revealing that the magnitude of θ is of the order of 10^{-3} deg. Microscopically, the NRR derives from the interference effect between electric dipole and magnetic dipole transitions, and theoretical calculations based on the crystal-field theory well explained the observed spectrum shape [41]. In this paper, we observe spatial distributions of NRR at two different photon energies, at which opposite directions of NRR are expected from the spectrum [22].

III. EXPERIMENTS

A. Sample preparation

Single crystals of Cr_2O_3 were grown by the laser floating-zone method. Powders of Cr_2O_3 were pressed into rods with a dimension of about 6 mm in diameter and 50 mm in length. The rods were sintered at 1200 °C for 72 h in air. The crystal growth was carried out on the sintered rods using a laser-based floating-zone furnace (Quantum Design LFZ1A) [42] at a feed rate of 35 mm/h under Ar at 5 atm. As a result, dark-green crystals were obtained and confirmed to be the corundum structure by x-ray diffraction (XRD) measurements. For measurements of optical properties, some of the crystals were oriented by using Laue XRD patterns, cut into thin plate shapes with the widest faces normal to the hexagonal c axis, and polished down to the thickness of about 20 μm . For measurements of the E -induced Faraday effect and the E -induced MCD, indium–tin oxide (ITO) was sputtered onto the widest faces of the plate-shaped samples to form a pair of transparent electrodes which allow the experimental setup with $\mathbf{k} \parallel \mathbf{E} \parallel c$.

B. Spectral measurements of optical absorption

The absorption spectrum of Cr_2O_3 was obtained by using a homebuilt fiber-based optical system in the photon-energy range of $1.58 \text{ eV} < E_{\text{ph}} < 2.48 \text{ eV}$. Unpolarized light from a tungsten-halogen lamp (AvaLight-HAL-S-MINI, Avantes) was incident on a sample along the c axis, and the transmitted light was detected by a spectrometer (Flame-S, Ocean Optics). The system was inserted into a commercial physical property measurement system (Quantum Design), which allows controlling the sample temperature. Although the sample was as thin as 20 μm , the spectra at $1.94 \text{ eV} < E_{\text{ph}} < 2.25 \text{ eV}$ could not be measured due to strong absorption [see Fig. 1(b)].

C. Spectral measurements of E -induced Faraday effect and E -induced MCD

Schematic illustrations of the optical setups for spectral measurements of the E -induced Faraday effect and the E -induced MCD are shown [see Figs. 7(a) and 7(b) in Appendix A]. A supercontinuum laser (SC-Pro, YSL Photonics) was used as a light source. Monochromatic light with a selected wavelength was obtained by using an acousto-optic wavelength tunable filter (AOTF-PRO, YSL Photonics). In the measurements of the E -induced Faraday effect, a sample is placed between a polarizer and an analyzer, where the angle between the transmission axes of the polarizer and analyzer is set at $\Theta = 45^\circ$. In the measurements of the E -induced MCD, right circularly polarized (RCP) or left circularly polarized (LCP) light is irradiated onto the sample by using a polarizer and a quarter-wave plate. For both measurements, signals were detected by a lock-in technique [14]. A sinusoidal voltage at a frequency of 999 Hz up to ± 100 V was applied to the sample, and the intensity of the transmitted light oscillating at the same frequency with the applied voltage was measured by using a lock-in amplifier (see also Appendix A). To obtain the spectra of the E -induced Faraday effect and the E -induced MCD, the signals were corrected at 2-nm wavelength intervals from 502 to 786 nm. The sample temperature was controlled by a liquid nitrogen flow cold stage.

D. Spatial distribution measurements of E -induced Faraday effect and E -induced MCD

Two-dimensional maps of the E -induced Faraday effect and the E -induced MCD were obtained by using a field-modulation imaging technique [43,44]. Schematic illustrations of the optical setups [see Figs. 7(c) and 7(d) in Appendix A] are shown. The polarization configurations are the same as those for the spectral measurements. In this technique, a square-wave voltage is applied to a sample, and transmission microscope images are captured by an scientific CMOS (sCMOS) camera (pco edge 5.5, Excelitas Technologies) alternatively under positive ($+V$) and negative ($-V$) voltage application. Then, the difference in signals under $+V$ and $-V$ [$\Delta I = I(+V) - I(-V)$] divided by the average of them (I) is calculated for each pixel of the camera. For the E -induced Faraday effect, when the polarization rotation angle $\phi = \beta V$ is sufficiently small as in the present case, $\Delta I/I$

is approximately proportional to ϕ and expressed as

$$\frac{\Delta I}{I} \cong \frac{4\pi}{180} \beta V. \quad (6)$$

Likewise, for the E -induced MCD, $\Delta I/I$ is approximately proportional to the magnitude of E -induced MCD and expressed as

$$\frac{\Delta I}{I} \cong 2\beta' V_c. \quad (7)$$

The calculation details are given in Appendix A. To obtain spatial distributions of small signals of $\Delta I/I$ with suppressing noises, large numbers (15 000) of $\Delta I/I$ maps are captured and averaged. A square-wave bias voltage (up to ± 100 V) was applied at a frequency of 20 or 30 Hz, and images were captured at 40 or 60 frames per second (fps). The spatial resolution of this field-modulation imaging technique is a few micrometers, and a $\Delta I/I$ signal of the order of 10^{-5} can be detected.

E. Spatial distribution measurements of NRR

Two-dimensional maps of NRR were obtained by using a polarization-modulation technique [45]. [See Fig. 7(e) in Appendix A for a schematic illustration of the optical setup.] In this technique, the polarization of the incident light is modulated by using a liquid-crystal variable retarder (LCC1223T-A, Thorlabs), and reflection microscope images with linearly polarized (I_{LP}) and right circularly polarized incident light (I_{RCP}) are captured alternatively. An analyzer whose transmission axis is 45° against the polarization direction of linearly polarized incident light is set behind the sample. In the approximation that the polarization rotation angle θ [deg] and circular dichroism of reflected light are small enough, θ is calculated as [45]

$$\frac{\Delta \tilde{I}}{\tilde{I}} = \frac{I_{LP} - I_{RCP}}{2I_{RCP}} \cong \frac{\pi}{180} \theta. \quad (8)$$

$\Delta \tilde{I}/\tilde{I}$ is calculated for each pixel of the camera, and large numbers (15 000) of $\Delta \tilde{I}/\tilde{I}$ maps are captured and averaged to detect small signals of θ . The polarization was modulated at a frequency of 20 Hz, and images were captured at 40 fps. However, even with this averaging process, finite backgrounds mainly due to sample tilting against the irradiated light remain, which prevent evaluating intrinsic NRR signals. To minimize such backgrounds, a $\Delta \tilde{I}/\tilde{I}$ map obtained at $T > T_N$ was subtracted from that obtained at $T < T_N$. Also, a 3×3 median filter was applied to the images to suppress noises.

IV. RESULTS AND DISCUSSION

A. Spectra of E -induced Faraday effect and E -induced MCD

Prior to the measurements, single-domain states of $L+$ and $L-$ were prepared by cooling the sample from $T > T_N$ while applying magnetic (\mathbf{H}) and electric (\mathbf{E}) fields. This ME cooling procedure stabilizes the $L+$ and $L-$ states when $H_c E_c > 0$ and $H_c E_c < 0$, respectively [46]. Here, H_c (E_c) represents \mathbf{H} (\mathbf{E}) along the c axis.

Figures 2(c)–2(f) show the spectra of E -induced Faraday effect and E -induced MCD obtained at 83 K after ME cooling with $\mu_0 H_c \approx +0.2$ T and E_c of opposite signs

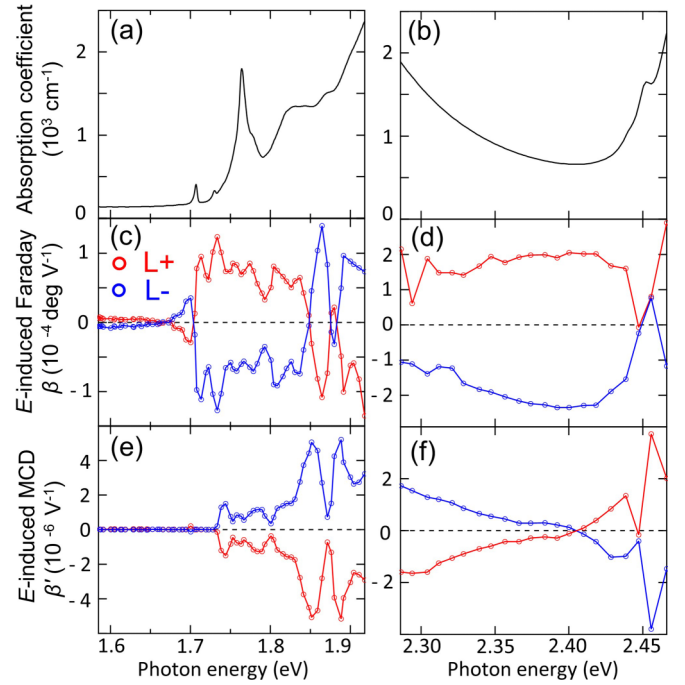


FIG. 2. Spectra of E -induced Faraday effect and E -induced MCD at 83 K. (a), (b) Enlarged absorption spectra in the geometry $\mathbf{k} \parallel c$ at $1.58 \text{ eV} < E_{\text{ph}} < 1.92 \text{ eV}$ [(a)] and $2.28 \text{ eV} < E_{\text{ph}} < 2.47 \text{ eV}$ [(b)]. (c)–(f) Spectra of E -induced Faraday effect [(c), (d)] and those of E -induced MCD [(e), (f)] in the geometry with $\mathbf{k} \parallel \mathbf{E} \parallel c$ at $1.58 \text{ eV} < E_{\text{ph}} < 1.92 \text{ eV}$ [(c), (e)] and $2.28 \text{ eV} < E_{\text{ph}} < 2.47 \text{ eV}$ [(d), (f)]. The red and blue dots correspond to the signals obtained in the single $L+$ and $L-$ domains, respectively. Note that each spectrum shows almost complete sign reversal against the domain switching.

[$+56 \text{ kV cm}^{-1}$ (red) and -56 kV cm^{-1} (blue)]. The cooling magnetic and electric fields were removed before the measurements. The spectra were measured in the visible region of $1.58 \text{ eV} < E_{\text{ph}} < 2.47 \text{ eV}$. However, at $1.92 \text{ eV} < E_{\text{ph}} < 2.28 \text{ eV}$, absorption was too strong to obtain meaningful signals. Thus, Fig. 2 displays the spectra at $1.58 \text{ eV} < E_{\text{ph}} < 1.92 \text{ eV}$ [Figs. 2(c) and 2(e)] and $2.28 \text{ eV} < E_{\text{ph}} < 2.47 \text{ eV}$ [Figs. 2(d) and 2(f)]. The spectra show almost complete sign reversals upon the reversal of the domain states [compare the red and blue dots in Figs. 2(c)–2(f)], which ensures that the spectra exactly reflect the E -induced Faraday effect and the E -induced MCD.

Now let us discuss the structures of the spectra. For the E -induced Faraday effect and the E -induced MCD in Cr_2O_3 , the spin-allowed transition to the excited state ${}^4T_{2g}$ from the ground state ${}^4A_{2g}$ is expected to give the largest contribution [16,47]. The broad absorption peak centered at 2.1 eV and extended from 1.7 to 2.4 eV corresponds to this transition [see Fig. 1(b)] [48]. Based on the crystal-field theory, ϕ and α_{MCD} around the peak are calculated as [16,17]

$$\phi \propto l\omega\Delta_E \left\{ \frac{\omega_C}{(\omega_C^2 - \omega^2)^2} - \frac{\omega_{A_1}}{(\omega_{A_1}^2 - \omega^2)^2} \right\} \quad \text{and} \quad (9)$$

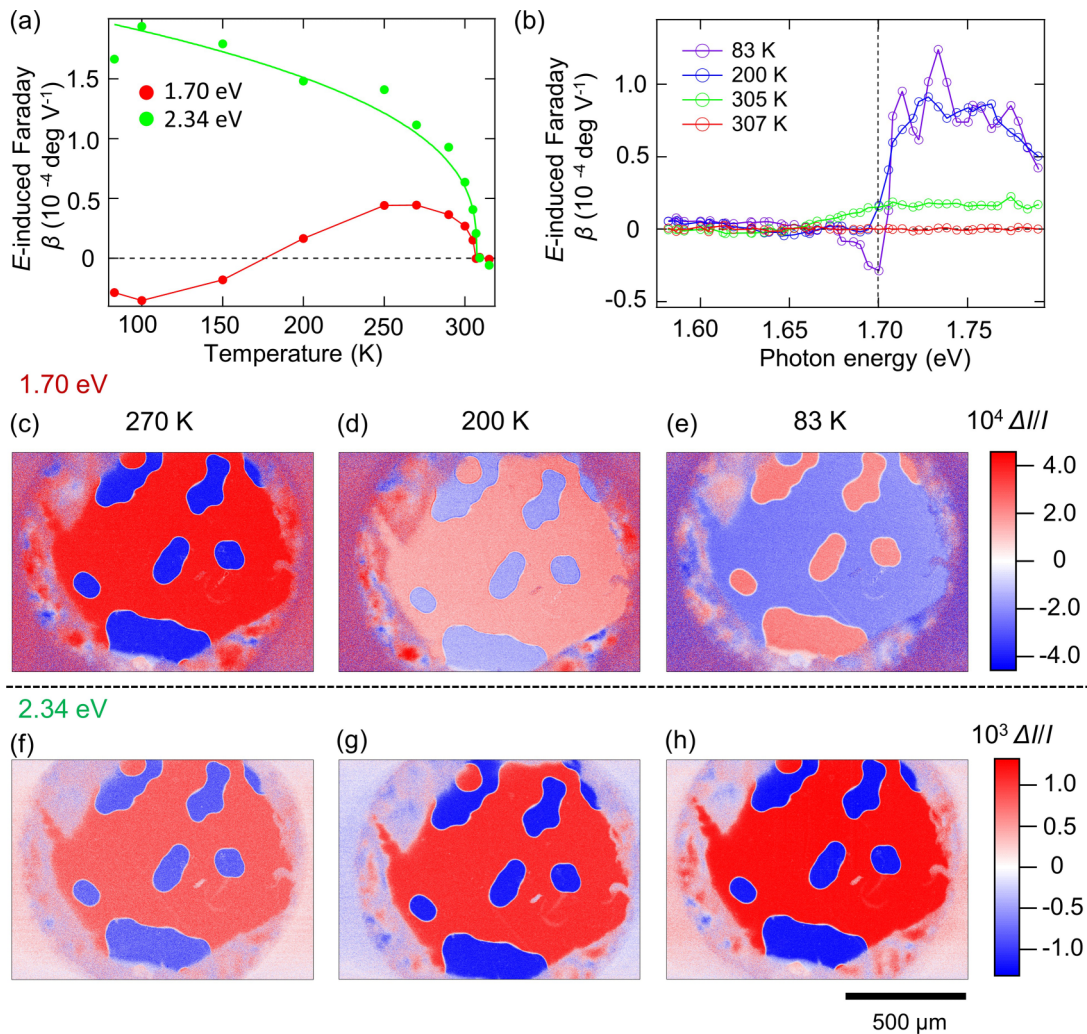


FIG. 3. Temperature (T) dependence and two-dimensional maps of the E -induced Faraday effect. (a) T dependence of the E -induced Faraday effect at $E_{\text{ph}} = 1.70$ eV (red dots) and 2.34 eV (green dots). The green curve is the fitting by the function of the AFM order parameter given in Eq. (11). The red line is a guide to the eye. (b) The spectra of the E -induced Faraday effect in the photon energy region of 1.58 eV $< E_{\text{ph}} < 1.80$ eV at 83 K (purple), 200 K (blue), 305 K (green), and 307 K (red). The dashed line denotes the photon energy of $E_{\text{ph}} = 1.70$ eV at which the characteristic T dependence was observed in (a). (c)–(h) Two-dimensional maps of the E -induced Faraday effect obtained with monochromatic light whose photon energies are $E_{\text{ph}} = 1.70$ eV (c)–(e) and $E_{\text{ph}} = 2.34$ eV (f)–(h). The maps were obtained at 270 K (c), (f), 200 K (d), (g), and 83 K (e), (h). In the red and blue regions, the signs of the E -induced Faraday effects are opposite to each other, and thus the contrasts correspond to the AFM domains.

$$\alpha_{\text{MCD}} \propto I\Gamma\Delta_E \left\{ \frac{\omega_C(\omega_C^2 + 3\omega^2)}{(\omega_C^2 - \omega^2)^3} - \frac{\omega_{A_1}(\omega_{A_1}^2 + 3\omega^2)}{(\omega_{A_1}^2 - \omega^2)^3} \right\}, \quad (10)$$

where ω is an angular frequency of incident light, Γ is a damping factor, $\hbar\omega_C$ ($\hbar\omega_{A_1}$) is the excitation energy to the $C(A_1)$ states, which is the split ${}^4T_{2g}$ state due to the trigonal field, the spin-orbit interaction, and the exchange interaction, and $\Delta_E \propto E_c$ is a shift of the energy states caused by applying an electric field. Details of the calculations are given in Appendix B. As discussed in Sec. II A, the E -induced Faraday effect and MCD involve the two contributions that originate from the ME coefficient α_{33} and the AFM order parameter l , the latter of which corresponds to Eqs. (9) and (10). It is

evident from these equations that the latter AFM contribution significantly enhances at around the resonance frequency ω_C (ω_{A_1}), thus dominating both ϕ and α_{MCD} . Also, these equations indicate that the spectrum of ϕ around the resonance frequencies is of dispersive type (i.e., exhibits a sign reversal), while that of α_{MCD} is of absorptive type (i.e., exhibits no sign reversal). As mentioned above, the spectra around the ${}^4T_{2g}$ peak centered at 2.1 eV were not obtained because of strong absorption. However, it is seen that the sign of the E -induced Faraday effect gets reversed between $E_{\text{ph}} < 2.1$ eV and $E_{\text{ph}} > 2.1$ eV, while that of E -induced MCD does not [compare the right end of Figs. 2(c) and 2(e) and the left end of Figs. 2(d) and 2(f)]. Thus, the obtained spectra do not contradict the calculations [Eqs. (9) and (10)].

The absorption peaks at 1.706 and 1.729, and 1.763 eV [see Fig. 2(a)] correspond to the spin-forbidden transitions

to the excited states of 2E_g and ${}^2T_{1g}$, respectively [48,49]. They can contribute to the E -induced Faraday effect and the E -induced MCD by the assistance of the spin-orbit interaction between these states and the ${}^4T_{2g}$ state [41]. Thus, peak structures observed at around 1.7–1.8 eV in Figs. 2(c) and 2(e) will derive from these spin-forbidden transitions. Relatively large and sharp peaks are also observed at around 1.8–1.9 eV in Figs. 2(c) and 2(e). Especially, the largest E -induced MCD of $5 \times 10^{-6} \text{ V}^{-1}$ is observed at 1.852 and 1.889 eV. These peaks will be related to the shoulder structures in the absorption spectrum at around 1.83–1.87 eV. However, the relationships between these shoulder structures and the electronic transitions are unclear [48].

Located between the two spin-allowed transitions of ${}^4T_{2g}$ and ${}^4T_{1g}$ [48], the spectra shown in Figs. 2(d) and 2(f) ($2.28 \text{ eV} < E_{\text{ph}} < 2.47 \text{ eV}$) are expected to be influenced by these transitions. As seen in Fig. 2(f), the E -induced MCD spectrum crosses the zero line at 2.405 eV. This may suggest that the ${}^4T_{1g}$ and ${}^4T_{2g}$ transitions have contributions of opposite signs to the E -induced MCD spectrum. The dispersive peak structure at around 2.45 eV in the E -induced MCD spectrum will correspond to the absorption peak at the same energy, which is assigned to the transition to the ${}^2T_{2g}$ state [48]. We note that the largest E -induced Faraday effect of about $2 \times 10^{-4} \text{ deg V}^{-1}$ is observed at $2.35 \text{ eV} < E_{\text{ph}} < 2.42 \text{ eV}$, which is about 15 to 20 times larger than those observed in the near-infrared region at around 100 K [16,17].

The spectra of the E -induced Faraday effect were measured at various temperatures. Figure 3(a) shows the T dependence at selected photon energies of 1.70 and 2.34 eV, while Fig. 3(b) shows the spectra in the photon energy range of $1.58 \text{ eV} < E_{\text{ph}} < 1.80 \text{ eV}$ at 83, 200, 305, and 307 K. These T profiles were obtained for the $L+$ single domain. As shown in Figs. 3(a) and 3(b), the signals vanish at 307 K ($\approx T_N$). When comparing the T profiles at 1.70 and 2.34 eV [compare the red and green dots in Fig. 3(a)], one can find that the latter one well obeys the T dependence of the AFM order parameter of Cr_2O_3 while the former one does not. The data at 2.34 eV are well fitted by the function of AFM order parameter [26,50]

$$l(T) = l_0(T_N - T)^{0.35} \quad (T < T_N), \quad (11)$$

as shown in the green curve in Fig. 3(a). Here, l_0 is a fitting parameter. On the other hand, the E -induced Faraday effect at 1.70 eV does not obey this function, and changes its sign at around 175 K. This is most likely because the photon energy of 1.70 eV corresponds to the energy at which the spin-forbidden transition-driven peak develops at low temperatures [see Fig. 3(b)]. As mentioned in Sec. II A, the T dependence of the E -induced Faraday effect is discussed in the context of competing contributions from the AFM order parameter l and the ME susceptibility α_{33} in Ref. [17]. However, such a discussion cannot be directly applied to the current case in which the development of the peak structures with decreasing temperature is clearly observed.

B. Antiferromagnetic domain observation

After characterizing the spectra of the E -induced Faraday effect and the E -induced MCD in Cr_2O_3 , we moved

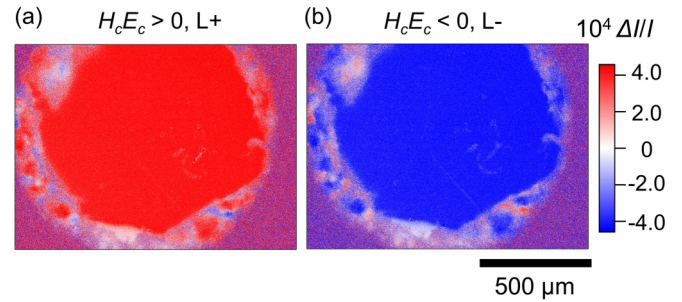


FIG. 4. Single domains obtained by the ME cooling. (a), (b) Two-dimensional map of the E -induced Faraday effect obtained by cooling the sample while applying magnetic and electric fields in the setting of $H_c E_c > 0$ (a) and $H_c E_c < 0$ (b). The domains in (a) and (b) correspond to the $L+$ and $L-$ domains, respectively.

on to the domain imaging using these effects. First, we utilized the E -induced Faraday effect. Figures 3(c)–3(h) show the two-dimensional maps of the E -induced Faraday effect obtained with using monochromatic LED light sources of 1.70 eV [Figs. 3(c)–3(e)] and 2.34 eV [Figs. 3(f)–3(h)]. The images obtained at 270 K [Figs. 3(c) and 3(f)], 200 K [Figs. 3(d) and 3(g)], and 83 K [Figs. 3(e) and 3(h)] are shown. In these images, clear contrasts of red (positive $\Delta I/I$) and blue (negative $\Delta I/I$) are observed. These contrasts correspond to positive and negative signs of the E -induced Faraday effects, and thus reflect the AFM domain structures. Consequently, we succeeded in the visualization of AFM domains using the E -induced Faraday effect. The typical domain size is several hundred micrometers, which is consistent with those obtained by other experimental techniques such as second-harmonic generation [34,40]. The contrasts obtained with the 2.34 eV LED light source become stronger with decreasing temperature [Figs. 3(f)–3(h)]. In contrast, those obtained with the 1.70 eV LED light source become weaker with decreasing temperature from 270 K and are reversed at 83 K [Figs. 3(c)–3(e)]. The observed T evolution of the domain contrasts is consistent with the result obtained by the spectral measurements shown in Fig. 3(a). The magnitudes of the E -induced Faraday effect calculated by using the $\Delta I/I$ averaged over single-domain areas are $\beta \approx 3 \times 10^{-5} \text{ deg V}^{-1}$ for 1.70 eV and $\beta \approx 1.8 \times 10^{-4} \text{ deg V}^{-1}$ for 2.34 eV at 83 K, which are well matched with those obtained by the spectral measurements [Fig. 3(a)].

We have also confirmed that the single-domain states of $L+$ or $L-$ are formed by the ME cooling. Figures 4(a) and 4(b) show the domains obtained by cooling the sample across T_N while applying magnetic and electric fields in the setting of $H_c E_c > 0$ and $H_c E_c < 0$, respectively. The magnitudes of the applied fields were $\mu_0 H_c \approx +0.2 \text{ T}$ and $E_c = \pm 56 \text{ kV cm}^{-1}$. The domain images were taken at 270 K with the 1.70 eV LED light source. The signals are uniform and the sign of them are opposite between the opposite ME cooling fields.

Next, we performed the domain imaging using the E -induced MCD effect. Figures 5(a) and 5(b) show the two-dimensional maps of the E -induced MCD obtained at 83 K with RCP and LCP incident light, respectively. Here, the 2.34 eV LED was used as a light source. In the images, clear contrasts of positive (red) and negative (blue) signals are

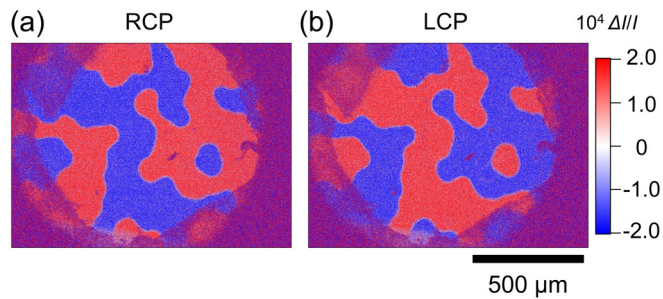


FIG. 5. Two-dimensional maps of the E -induced MCD effect obtained with right (a) and left (b) circularly polarized monochromatic light whose photon energy is $E_{\text{ph}} = 2.34$ eV. These images were taken at 83 K.

observed, which reflect the AFM domain structures. The contrast reversal between the RCP and LCP incident light supports that the obtained signals come from the E -induced MCD. Thus, we show that the spatial distribution measurement of the E -induced MCD is also effective to visualize AFM domains of Cr_2O_3 . The magnitude obtained in this measurement was $\beta' \approx 9 \times 10^{-5} \text{ V}^{-1}$, which is well matched with that obtained by the spectral measurement [Fig. 2(f)].

Finally, we performed spatial distribution measurements of NRR. Figures 6(a) and 6(b) show the two-dimensional maps of NRR obtained at 270 K with monochromatic light whose photon energies are 2.10 and 1.91 eV, respectively. Even with the background-suppressing process described in Sec. III E, finite backgrounds with some slopes remain. To show the whole domain structures, the color scale is set about 10 times larger than the actual rotation angle. Between the bright and dark regions in these images, the directions of the polarization rotation of the reflected light are opposite. Thus, the contrasts reflect the AFM domain structures. Contrast reversal between the images obtained with 2.10 and 1.91 eV light is clearly observed [compare Figs. 6(a) and 6(b)], which is consistent with the previously reported NRR spectrum [22]. The magnitude of the rotation was calculated by the differences of θ between the adjacent opposite domains. The calculated angles are $|\theta| \approx 3 \times 10^{-3}$ deg for both energies, which are

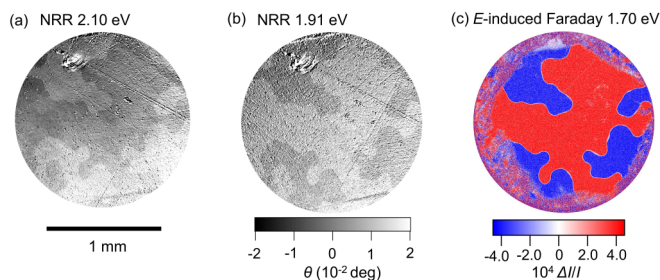


FIG. 6. Two-dimensional maps of NRR. (a), (b) AFM domain visualized by using NRR with monochromatic light whose photon energies are 2.10 eV (a) and 1.91 eV (b). The contrasts are reversed between the two. (c) Antiferromagnetic domains visualized by using the E -induced Faraday effect with monochromatic light whose photon energy is 1.70 eV at the same position with (a), (b). The obtained domains were perfectly matched with (a), (b). These images were taken at 270 K.

also consistent with the previous work [22]. Furthermore, a two-dimensional map of the E -induced Faraday effect was obtained for the same sample [Fig. 6(c)]. The domain patterns obtained by using NRR and the E -induced Faraday effect are exactly the same. Considering that the penetration depth of light with a photon energy of 2.10 eV is expected to be less than $2 \mu\text{m}$ from the absorption spectrum, the NRR maps show the domain structures near the sample surface. Thus, the same domain patterns obtained by NRR and the E -induced Faraday effect indicate that the domains are uniform in the thickness direction.

V. SUMMARY

In summary, we have investigated nonreciprocal optical effects [electric field-induced (E -induced) Faraday effect, the electric field-induced magnetic circular dichroism (E -induced MCD), and the spontaneous nonreciprocal rotation of reflected light (NRR)] in Cr_2O_3 focusing on their spectra and spatial distributions. The spectral measurements of E -induced Faraday effect and E -induced MCD show that relatively large effects appear at frequencies around the transition to the ${}^4T_{2g}$ states. In our bulk samples, the effects at the center energy of the transition could not be obtained due to strong absorption. Since magnitudes of these E -induced nonreciprocal optical effects are independent of the sample thickness, it will be an interesting future work to measure the effects at the peak center in thin-film samples.

So far, the smallness of the nonreciprocal optical effects studied here has prevented antiferromagnetic-domain observation via their spatial distribution measurements. In our measurements, however, by adopting the field- and polarization-modulation imaging techniques, antiferromagnetic domains were clearly visualized by utilizing these effects. We showed that antiferromagnetic domains of Cr_2O_3 can be visualized both in the transmission (E -induced Faraday effect and E -induced MCD) and reflection (NRR) settings. Furthermore, NRR is a spontaneous effect, and the application of an electric field is unnecessary for its measurement. Thus, these methods can be widely applied to the visualization of antiferromagnetic domains of diagonal ME materials regardless of their transparency, reflectivity, and electrical conductivity.

ACKNOWLEDGMENTS

We thank S. Hirose for his help with sputtering ITO at the early stage of this research. We also thank Y. Uemura, S. Matsuoka, and T. Hasegawa for their help with establishment of the field-modulation imaging system. The images of crystal structures were drawn using the software VESTA [51]. This work was supported by World-leading Innovative Graduate Study Program for Materials Research, Industry, and Technology (MERIT-WINGS) of the University of Tokyo, the MEXT Leading Initiative for Excellent Young Researchers (LEADER), and by JSPS KAKENHI Grants No. JP19H05823, No. JP19H01847, No. JP21H04436, No. JP21H04988, and No. JP22J11247.

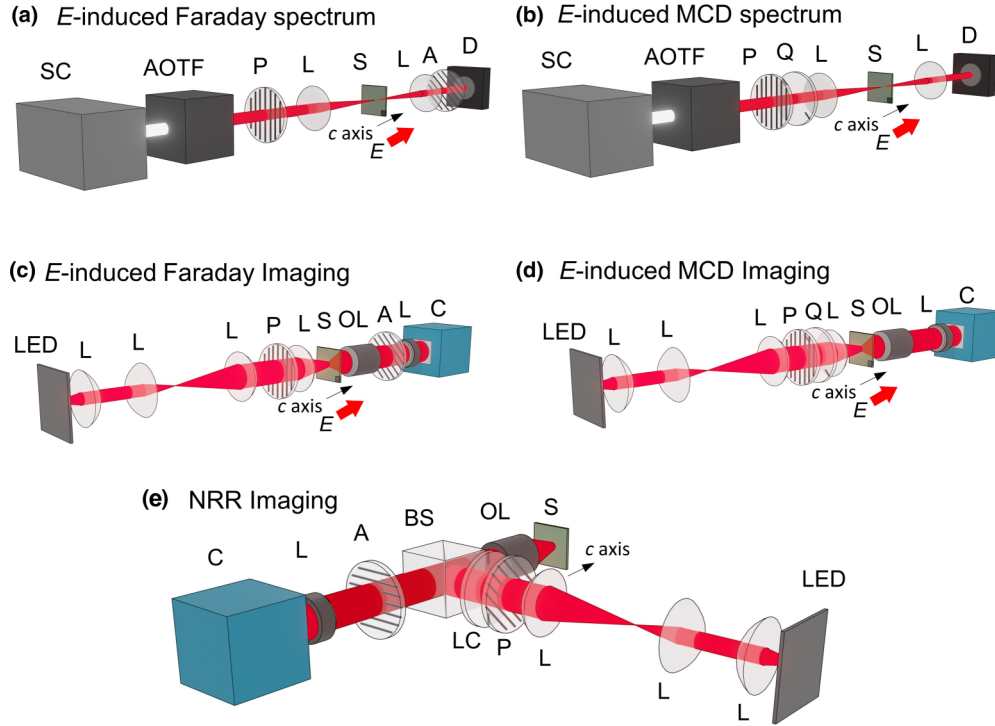


FIG. 7. Schematic illustrations of the optical setups. (a), (b) The optical setups for the spectral measurements of *E*-induced Faraday effect (a) and *E*-induced MCD (b). (c)–(e) Those for the spatial distribution measurements of *E*-induced Faraday effect (c), *E*-induced MCD (d), and NRR (e) are depicted. The red arrows in (a)–(d) indicate the directions of an applied electric field. Note that in the measurements of NRR, an electric field is not applied. SC: Supercontinuum laser; AOTF: Acousto-optic wavelength tunable filter; P: Polarizer; L: Lens; S: Sample; A: Analyzer; D: Si detector; Q: Quarter-wave plate; LED: LED light source; OL: Objective lens; C: sCMOS camera; LC: Liquid-crystal variable retarder; BS: Beam splitter.

APPENDIX A: DETAILS OF OPTICAL MEASUREMENTS

Figure 7 shows schematic illustrations of the optical setups used for the spectral measurements of the electric field-induced (*E*-induced) Faraday effect [Fig. 7(a)] and the electric field-induced magnetic circular dichroism (*E*-induced MCD) [Fig. 7(b)], and the spatial distribution measurements of *E*-induced Faraday effect [Fig. 7(c)], *E*-induced MCD [Fig. 7(d)], and nonreciprocal rotation of reflected light (NRR) [Fig. 7(e)]. In the following subsections, we describe the calculation details of each measurement method.

1. Measurements of *E*-induced Faraday effect

When the angle between the transmission axes of the polarizer and the analyzer is set at $\Theta = 45^\circ$, the intensity of light transmitted through a material which exhibits the *E*-induced Faraday effect is given by

$$I = \frac{I_0}{2} \{\sin(2\phi) + 1\}, \quad (\text{A1})$$

where I_0 is the intensity of transmitted light at parallel-Nicols setting and ϕ [deg] is the rotation angle of the polarization plane induced by applying an electric field. Because the *E*-induced Faraday effect is usually a small effect, it can be assumed that $\sin(2\phi) \approx \frac{2\pi}{180}\phi$ and Eq. (A1) is rewritten as

$$I \approx I_0 \left(\frac{\pi}{180} \beta V + \frac{1}{2} \right), \quad (\text{A2})$$

where β [deg V⁻¹] is the coefficient representing the magnitude of the *E*-induced Faraday effect and V [V] is an applied voltage.

In the spectral measurements, a sinusoidal voltage $V_0 \sin(\omega t)$ at a frequency of 999 Hz is applied, and the intensity of the transmitted light oscillating at the same frequency with the applied voltage $\frac{\pi}{180} I_0 \beta V_0$ was detected by using a lock-in amplifier [14]. The coefficient β is calculated by dividing the AC component by the DC component, $I_0/2$.

In the spatial distribution measurements, the field-modulation imaging technique [43,44] is applied. A square-wave voltage is applied to a sample, and transmission microscope images are captured by a sCMOS camera alternatively under positive (+ V) and negative (− V) voltage application. Then, the difference in signals under + V and − V [$\Delta I = I(+V) - I(-V)$] divided by the average of them (I) is calculated for each pixel of the camera as

$$\begin{aligned} \frac{\Delta I}{I} &= \frac{I_0 \left(\frac{2\pi}{180} \beta (+V) + \frac{1}{2} \right) - I_0 \left(\frac{2\pi}{180} \beta (-V) + \frac{1}{2} \right)}{\left\{ I_0 \left(\frac{2\pi}{180} \beta (+V) + \frac{1}{2} \right) + I_0 \left(\frac{2\pi}{180} \beta (-V) + \frac{1}{2} \right) \right\} / 2} \\ &= \frac{4\pi}{180} \beta V. \end{aligned} \quad (\text{A3})$$

To obtain spatial distributions of small signals of $\Delta I/I$ with suppressing noises, large numbers (15 000) of $\Delta I/I$ maps are captured and averaged.

2. Measurements of E -induced MCD

When right or left circularly polarized light (RCP or LCP) is irradiated onto a material which exhibits E -induced MCD, the intensity of transmitted light $I_{\text{RCP, LCP}}$ is described as

$$I_{\text{RCP, LCP}} = I_0 \exp\{-(\alpha_0 \mp \beta' E)d\}, \quad (\text{A4})$$

where I_0 is the intensity of incident light, α_0 [cm^{-1}] is an absorption coefficient for RCP and LCP light in zero electric field, β' [V^{-1}] is the coefficient representing the magnitude of E -induced MCD, E [V cm^{-1}] is an applied electric field, and d [cm] is a sample thickness. Here, the sign of \pm depends on the helicity of incident light. Since E -induced MCD is usually small, Eq. (A4) can be assumed as

$$I_{\text{RCP, LCP}} \approx I_0 e^{-\alpha_0 d} (1 \pm \beta' E d) = I_0 e^{-\alpha_0 d} (1 \pm \beta' V), \quad (\text{A5})$$

where V [V] is an applied voltage.

In the spectral measurements, a sinusoidal voltage $V_0 \sin(\omega t)$ at a frequency of 999 Hz is applied, and the intensity of the transmitted light oscillating at the same frequency with the applied voltage $\delta I_{\text{RCP, LCP}} = \pm I_0 e^{-\alpha_0 d} \beta' V_0$ was detected by using a lock-in amplifier. The coefficient β' is calculated as

$$\beta' = \frac{\left(\frac{\delta I_{\text{RCP}}}{I_0 e^{-\alpha_0 d} V_0} - \frac{\delta I_{\text{LCP}}}{I_0 e^{-\alpha_0 d} V_0}\right)}{2}. \quad (\text{A6})$$

In the spatial distribution measurements, in the same manner as measurements of the E -induced Faraday effect, the field-modulation imaging technique is applied. Here, $\Delta I/I$ is calculated for each pixel of the camera as

$$\frac{\Delta I}{I} = \frac{I_0 e^{-\alpha_0 d} (1 \pm \beta' (+V)) - I_0 e^{-\alpha_0 d} (1 \pm \beta' (-V))}{\{I_0 e^{-\alpha_0 d} (1 \pm \beta' (+V)) + I_0 e^{-\alpha_0 d} (1 \pm \beta' (-V))\}/2} = \pm 2\beta' V, \quad (\text{A7})$$

where the sign of \pm depends on the helicity of incident light. The averaged images of $\Delta I/I$ were taken both under RCP and LCP light irradiation, and the contrast reversal between the two images was confirmed (see Fig. 5).

3. Measurements of NRR

The spatial distribution measurements of NRR were performed by adopting the polarization-modulation imaging technique [45]. Figure 7(e) shows a schematical illustration of the optical setup. Here, the transmission axis of the analyzer and the fast axis of the liquid-crystal variable retarder is set at 45° against the transmission axis of the polarizer. The polarization of incident light, i.e., linearly polarized (LP), RCP, and LCP, can be switched by tuning a voltage applied to the liquid-crystal variable retarder. In this setting, when LP, RCP, or LCP light is irradiated onto a material which exhibits NRR, the intensities of reflected light (I_{LP} , I_{RCP} , and I_{LCP}) are described as [45]

$$I_{\text{LP}} = \frac{1}{2} |\sin \theta - i\varepsilon \cos \theta + (\cos \theta + i\varepsilon \sin \theta)|^2 I_0, \quad (\text{A8})$$

$$I_{\text{RCP}} = \frac{1}{2} |\sin \theta - i\varepsilon \cos \theta + i(\cos \theta + i\varepsilon \sin \theta)|^2 I_0, \quad (\text{A9})$$

$$I_{\text{LCP}} = \frac{1}{2} |\sin \theta - i\varepsilon \cos \theta - i(\cos \theta + i\varepsilon \sin \theta)|^2 I_0, \quad (\text{A10})$$

where θ [rad] is a rotation angle and ε [rad] is the ellipticity of reflected light, I_0 is the intensity of incident light. Then, θ

can be calculated as

$$\theta = \frac{1}{2} \sin^{-1} \frac{2I_{\text{LP}} - (I_{\text{RCP}} + I_{\text{LCP}})}{(1 - \varepsilon^2)I_0}. \quad (\text{A11})$$

When θ and ε are small enough and the absorption of the material is neglected, Eq. (A11) can be assumed as

$$\theta \approx \frac{2I_{\text{LP}} - (I_{\text{RCP}} + I_{\text{LCP}})}{2(1 - \varepsilon^2)(I_{\text{RCP}} + I_{\text{LCP}})} \approx \frac{I_{\text{LP}} - I_{\text{RCP}}}{2I_{\text{RCP}}} = \frac{\Delta \tilde{I}}{\tilde{I}}. \quad (\text{A12})$$

Equation (8) is shown in the [deg] unit. $\Delta \tilde{I}/\tilde{I}$ is calculated for each pixel of the camera, and large numbers (15 000) of $\Delta \tilde{I}/\tilde{I}$ maps are captured and averaged to detect small signals of θ .

APPENDIX B: CALCULATIONS OF FREQUENCY DEPENDENCE OF E -INDUCED FARADAY EFFECT AND E -INDUCED MCD

The optical transitions from the ground state $^4A_{2g}$ to the excited state $^4T_{2g}$ largely contribute to the E -induced Faraday effect and E -induced MCD in Cr_2O_3 [16,47]. The contribution to the complex Faraday rotation from the Cr^{3+} ion at site A [see Fig. 1(a)], $\Phi_A(\omega)$, is provided as [16,47]

$$\Phi_A(\omega) = \frac{2\pi\omega}{n\hbar c} p_\alpha^2 (\omega - i\Gamma_\alpha) \left\{ \frac{1}{(\omega_{C(\alpha)g}^2 - \omega^2 + \Gamma_\alpha^2) + 2i\omega\Gamma_\alpha} - \sum_{i=1,2,3} \frac{a_{A_i}^2(\alpha)}{(\omega_{A_i(\alpha)g}^2 - \omega^2 + \Gamma_\alpha^2) + 2i\omega\Gamma_\alpha} \right\}, \quad (\text{B1})$$

where ω is an angular frequency of incident light, $n = (n_+ + n_-)/2$ is the averaged complex refractive index of RCP (n_+) and LCP (n_-) light, p_α^2 is the average dipole moment for the transition from the ground state $^4A_{2g}$ to the excited state $^4T_{2g}$, α represents a spin configuration, Γ is a damping factor, $\hbar\omega_{C, A_i(\alpha)g}$ is the excitation energies to the C and A_i states, which are the split 4T_2 state due to the trigonal field, the spin-orbit interaction, and the exchange interaction, $a_{A_i}^2(\alpha)$ is the occupation probability of the A_i state. The real and imaginary parts of $\Phi_A(\omega)$ correspond to the Faraday rotation and magnetic circular dichroism, respectively.

When an electric field is not applied, the Cr^{3+} ion at site B exhibits the same magnitude but opposite sign contribution, and thus spontaneous Faraday effect is forbidden. Under an electric field along the c axis (E_c), finite magnetization is induced, i.e., $m_A + m_B \neq 0$, where m_A (m_B) is magnetization at site A (B). In addition, the ground- and excited states are shifted (called pseudo-Stark shift [16,52]), which makes the excitation energies of $\hbar\omega_{C, A_i(\alpha)g}$ distinct between the site A and B as

$$\omega_{C, A_i g}^{A(B)} = \omega_{C, A_i(\alpha)g} \pm |A_1^0| (\chi_0 + \chi_{C, A_i}) E_c, \approx \omega_{C, A_i(\alpha)g} \pm \Delta_E \quad (\text{B2})$$

where A_1^0 is the magnitude of the odd trigonal field, χ_0 and χ_{C, A_i} are coefficients which represent mixing of the wave functions of the states of opposite parity with the wave functions of the ground and excited (C, A_i) states, respectively, by the odd trigonal field. Here, we assumed that $\chi_C \approx \chi_{A_i}$ and Δ_E represents the effects of an applied electric field. The sign of \pm depends on the site A or B .

Then, the contributions from the Cr^{3+} ions at sites A and B are calculated as

$$\begin{aligned}
 m_A \Phi_A(\omega) + m_B \Phi_B(\omega) = & m_A \frac{2\pi\omega}{\hbar c} p_\alpha^2(\omega - i\Gamma_\alpha) \left\{ \frac{1}{((\omega_{C(\alpha)g} + \Delta_E)^2 \pm \Delta_E \omega^2 + \Gamma_\alpha^2) + 2i\omega\Gamma_\alpha} \right. \\
 & \left. - \sum_{i=1,2,3} \frac{a_{A_i}^2(\alpha)}{((\omega_{A_i(\alpha)g} + \Delta_E)^2 - \omega^2 + \Gamma_\alpha^2) + 2i\omega\Gamma_\alpha} \right\} \\
 & + m_B \frac{2\pi\omega}{\hbar c} p_\alpha^2(\omega - i\Gamma_\alpha) \left\{ \frac{1}{((\omega_{C(\alpha)g} - \Delta_E)^2 \pm \Delta_E \omega^2 + \Gamma_\alpha^2) + 2i\omega\Gamma_\alpha} \right. \\
 & \left. - \sum_{i=1,2,3} \frac{a_{A_i}^2(\alpha)}{((\omega_{A_i(\alpha)g} - \Delta_E)^2 - \omega^2 + \Gamma_\alpha^2) + 2i\omega\Gamma_\alpha} \right\}. \quad (\text{B3})
 \end{aligned}$$

In the following calculation, we shall assume that the effect of the trigonal field is much greater than the spin-orbit interaction for the splitting of the ${}^4T_{2g}$ state and $a_{A_2}^2(\alpha) = a_{A_3}^2(\alpha) = 0$ [16]. We shall also assume that the damping factor Γ_α and the effect of pseudo-Stark shift are small and $\Gamma_\alpha^2, \Delta_E^2 \approx 0$. Under these assumptions, the real part (Re) and imaginary part (Im) of Eq. (B3) are given as

$$\text{Re(B2)} \approx \frac{2\pi\omega^2}{\hbar c} p_\alpha^2 \left[(m_A + m_B) \left(\frac{1}{\omega_{C(\alpha)g}^2 - \omega^2} - \frac{1}{\omega_{A_1(\alpha)g}^2 - \omega^2} \right) - (m_A - m_B) \left(\frac{2\Delta_E \omega_{C(\alpha)g}}{(\omega_{C(\alpha)g}^2 - \omega^2)^2} - \frac{2\Delta_E \omega_{A_1(\alpha)g}}{(\omega_{A_1(\alpha)g}^2 - \omega^2)^2} \right) \right], \quad (\text{B4})$$

$$\begin{aligned}
 \text{Im(B2)} \approx & \frac{2\pi\omega}{\hbar c} p_\alpha^2 \Gamma_\alpha \left[(m_A + m_B) \left(\frac{\omega_{C(\alpha)g}^2 + \omega^2}{(\omega_{C(\alpha)g}^2 - \omega^2)^2} - \frac{\omega_{A_1(\alpha)g}^2 + \omega^2}{(\omega_{A_1(\alpha)g}^2 - \omega^2)^2} \right) \right. \\
 & \left. - (m_A - m_B) \left(\frac{2\Delta_E \omega_c (\omega_c^2 + 3\omega)^2}{(\omega_{C(\alpha)g}^2 - \omega^2)^3} - \frac{2\Delta_E \omega_{A_1(\alpha)g} (\omega_{A_1(\alpha)g}^2 + 3\omega)^2}{(\omega_{A_1(\alpha)g}^2 - \omega^2)^3} \right) \right]. \quad (\text{B5})
 \end{aligned}$$

As shown in these equations, at an angular frequency near $\omega_{C, A_i(\alpha)g}$, the effect from the antiferromagnetic order parameter $l = m_A - m_B$ is dominant both for the real and imaginary parts of Eq. (B3). The contribution to the Faraday effect from a unit cell is given by $2(m_A \Phi_A(\omega) + m_B \Phi_B(\omega))$, and a general expression can be obtained by summing it over all the spin states and the number of unit cells in a crystal. Thus, the E -induced Faraday effect and E -induced MCD as a function of frequency are obtained as Eqs. (9) and (10), respectively.

-
- [1] G. L. J. A. Rikken, C. Strohm, and P. Wyder, Observation of Magnetoelectric Directional Anisotropy, *Phys. Rev. Lett.* **89**, 133005 (2002).
- [2] J. H. Jung, M. Matsubara, T. Arima, J. P. He, Y. Kaneko, and Y. Tokura, Optical Magnetoelectric Effect in the Polar GaFeO₃ Ferrimagnet, *Phys. Rev. Lett.* **93**, 037403 (2004).
- [3] T. Arima, Magneto-electric optics in non-centrosymmetric ferromagnets, *J. Phys.: Condens. Matter* **20**, 434211 (2008).
- [4] M. Saito, K. Taniguchi, and T. Arima, Gigantic optical magnetoelectric effect in CuB₂O₄, *J. Phys. Soc. Jpn.* **77**, 013705 (2008).
- [5] I. Kézsmárki, N. Kida, H. Murakawa, S. Bordács, Y. Onose, and Y. Tokura, Enhanced Directional Dichroism of Terahertz Light in Resonance with Magnetic Excitations of the Multiferroic Ba₂CoGe₂O₇ Oxide Compound, *Phys. Rev. Lett.* **106**, 057403 (2011).
- [6] Y. Takahashi, R. Shimano, Y. Kaneko, H. Murakawa, and Y. Tokura, Magnetoelectric resonance with electromagnons in a perovskite helimagnet, *Nat. Phys.* **8**, 121 (2012).
- [7] D. Szaller, S. Bordács, and I. Kézsmárki, Symmetry conditions for nonreciprocal light propagation in magnetic crystals, *Phys. Rev. B* **87**, 014421 (2013).
- [8] M. Akaki, K. Kimura, Y. Kato, Y. Sawada, Y. Narumi, H. Ohta, T. Kimura, Y. Motome, and M. Hagiwara, Nonreciprocal linear dichroism observed in electron spin resonance spectra of the magnetoelectric multiferroic Pb(TiO)Cu₄(PO₄)₄, *Phys. Rev. Res.* **3**, L042043 (2021).
- [9] K. Park, M. O. Yokosuk, M. Goryca, J. J. Yang, S. A. Crooker, S. W. Cheong, K. Haule, D. Vanderbilt, H. -S. Kim, and J. L. Musfeldt, Nonreciprocal directional dichroism at telecom wavelengths, *npj Quantum Mater.* **7**, 38 (2022).
- [10] V. Kocsis, K. Penc, T. Rődm, U. Nagel, J. Vít, J. Romhányi, Y. Tokunaga, Y. Taguchi, Y. Tokura, I. Kézsmárki, and S. Bordács, Identification of Antiferromagnetic Domains via the Optical Magnetoelectric Effect, *Phys. Rev. Lett.* **121**, 057601 (2018).
- [11] K. Kimura, T. Katsuyoshi, Y. Sawada, S. Kimura, and T. Kimura, Imaging switchable magnetoelectric quadrupole domains via nonreciprocal linear dichroism, *Commun. Mater.* **1**, 39 (2020).
- [12] T. Sato, N. Abe, Y. Tokunaga, and T. Arima, Antiferromagnetic domain wall dynamics in magnetoelectric MnTiO₃ studied by optical imaging, *Phys. Rev. B* **105**, 094417 (2022).

- [13] K. Kimura, Y. Otake, and T. Kimura, Visualizing rotation and reversal of the Néel vector through antiferromagnetic trichroism, *Nat. Commun.* **13**, 697 (2022).
- [14] T. H. O'Dell and E. A. D. White, Electric field induced Faraday rotation in chromic oxide, *Philos. Mag. A: J. Theor. Exp. Appl. Phys.* **22**, 649 (1970).
- [15] B. B. Krichevstov, V. V. Pavlov, and R. V. Pisarev, Non-reciprocal rotation of the polarization plane of light in the antiferromagnet Cr_2O_3 which is linear and quadratic in the electric field, *Pis'ma Zh. Eksp. Teor. Fiz.* **44**, 471 (1986) [*Sov. J. Exp. Theor. Phys. Lett.* **44**, 607 (1986)].
- [16] B. B. Krichevstov, V. V. Pavlov, and R. V. Pisarev, Nonreciprocal optical effects in antiferromagnetic Cr_2O_3 subjected to electric and magnetic fields, *Zh. Eksp. Teor. Fiz.* **94**, 284 (1988) [*Sov. Phys. JETP* **67**, 378 (1988)].
- [17] J. Wang and C. Binek, Dispersion of Electric-Field-Induced Faraday Effect in Magnetoelectric Cr_2O_3 , *Phys. Rev. Appl.* **5**, 031001 (2016).
- [18] R. Hikita, H. Taniguchi, T. Shinkai, and T. Kohmoto, Dynamics of the electric-field induced magnetization in antiferromagnetic chromium oxide observed by Faraday rotation, *J. Phys. Conf. Ser.* **1220**, 012017 (2019).
- [19] K. Fujimoto, T. Hasunuma, and T. Kohmoto, Electric-field induced magnetization in YIG observed by Faraday rotation, *J. Phys. Conf. Ser.* **1220**, 012055 (2019).
- [20] R. M. Hornreich and S. Shtrikman, Theory of gyrotropic birefringence, *Phys. Rev.* **171**, 1065 (1968).
- [21] B. B. Krichevstov, V. V. Pavlov, R. V. Pisarev, and V. N. Gridnev, Spontaneous non-reciprocal reflection of light from antiferromagnetic Cr_2O_3 , *J. Phys.: Condens. Matter* **5**, 8233 (1993).
- [22] B. B. Krichevstov, V. V. Pavlov, R. V. Pisarev, and V. N. Gridnev, Magnetoelectric Spectroscopy of Electronic Transitions in Antiferromagnetic Cr_2O_3 , *Phys. Rev. Lett.* **76**, 4628 (1996).
- [23] S.-W. Cheong, S. Lim, K. Du, and F.-T. Huang, Permutable SOS (symmetry operational similarity), *npj Quantum Mater.* **6**, 58 (2021).
- [24] S.-W. Cheong, Trompe l'oeil ferromagnetism, *npj Quantum Mater.* **5**, 37 (2020).
- [25] W. F. Brown, S. Shtrikman, and D. Treves, Possibility of visual observation of antiferromagnetic domains, *J. Appl. Phys.* **34**, 1233 (1963).
- [26] R. V. Pisarev, B. B. Krichevstov, and V. V. Pavlov, Optical study of the antiferromagnetic-paramagnetic phase transition in chromium oxide Cr_2O_3 , *Phase Transitions* **37**, 63 (1991).
- [27] A. M. Kuzmenko, V. Dziom, A. Shuvaev, A. Pimenov, D. Szaller, A. A. Mukhin, V. Y. Ivanov, and A. Pimenov, Sign change of polarization rotation under time or space inversion in magnetoelectric $\text{YbAl}_3(\text{BO}_3)_4$, *Phys. Rev. B* **99**, 224417 (2019).
- [28] S. Iguchi, R. Masuda, S. Seki, Y. Tokura, and Y. Takahashi, Enhanced gyrotropic birefringence and natural optical activity on electromagnon resonance in a helimagnet, *Nat. Commun.* **12**, 6674 (2021).
- [29] I. E. Dzyaloshinskii, On the magneto-electrical effect in antiferromagnetics, *Zh. Exp. Teor. Fiz.* **33**, 881 (1959) [*Sov. Phys. JETP* **10**, 628 (1960)].
- [30] D. N. Astrov, The magnetoelectric effect in antiferromagnetics, *Zh. Exp. Teor. Fiz.* **38**, 984 (1960) [*Sov. Phys. JETP* **11**, 708 (1960)].
- [31] T. R. McGuire, E. J. Scott, and F. H. Grannis, Antiferromagnetism in a Cr_2O_3 crystal, *Phys. Rev.* **102**, 1000 (1956).
- [32] L. M. Corliss, J. M. Hastings, R. Nathans, and G. Shirane, Magnetic structure of Cr_2O_3 , *J. Appl. Phys.* **36**, 1099 (1965).
- [33] E. Kita, A. Tasaki, and K. Siratori, Application of SQUID magnetometer to the measurement of magnetoelectric effect in Cr_2O_3 , *Jpn. J. Appl. Phys.* **18**, 1361 (1979).
- [34] M. Fiebig, D. Fröhlich, G. Sluyterman v. L., and R. V. Pisarev, Domain topography of antiferromagnetic Cr_2O_3 by second harmonic generation, *Appl. Phys. Lett.* **66**, 2906 (1995).
- [35] P. Schoenherr, L. M. Giraldo, M. Lilienblum, M. Trassin, D. Meier, and M. Fiebig, Magnetoelectric force microscopy on antiferromagnetic 180° domains in Cr_2O_3 , *Materials* **10**, 1051 (2017).
- [36] N. Wu, X. He, A. L. Wysocki, U. Lanke, T. Komesu, K. D. Belashchenko, C. Binek, and P. A. Dowben, Imaging and Control of Surface Magnetization Domains in a Magnetoelectric Antiferromagnet, *Phys. Rev. Lett.* **106**, 087202 (2011).
- [37] Y. Shiratsuchi, S. Watanabe, H. Yoshida, N. Kishida, R. Nakatani, Y. Kotani, K. Toyoki, and T. Nakamura, Observation of the magnetoelectric reversal process of the antiferromagnetic domain, *Appl. Phys. Lett.* **113**, 242404 (2018).
- [38] P. Appel, B. J. Shields, T. Kosub, N. Hedrich, R. Hübner, J. Faßbender, D. Makarov, and P. Maletinsky, Nanomagnetism of magnetoelectric granular thin-film antiferromagnets, *Nano Lett.* **19**, 1682 (2019).
- [39] N. Hedrich, K. Wagner, O. V. Pylypovskiy, B. J. Shields, T. Kosub, D. D. Sheka, D. Makarov, and P. Maletinsky, Nanoscale mechanics of antiferromagnetic domain walls, *Nat. Phys.* **17**, 574 (2021).
- [40] M. S. Wörnle, P. Welter, M. Giraldo, T. Lottermoser, M. Fiebig, P. Gambardella, and C. L. Degen, Coexistence of Bloch and Néel walls in a collinear antiferromagnet, *Phys. Rev. B* **103**, 094426 (2021).
- [41] M. Muto, Y. Tanabe, T. Iizuka-Sakano, and E. Hanamura, Magnetoelectric and second-harmonic spectra in antiferromagnetic Cr_2O_3 , *Phys. Rev. B* **57**, 9586 (1998).
- [42] Y. Kaneko and Y. Tokura, Floating zone furnace equipped with a high power laser of 1 KW composed of five smart beams, *J. Cryst. Growth* **533**, 125435 (2020).
- [43] Y. Uemura, S. Arai, J. Tsutsumi, S. Matsuoka, H. Yamada, R. Kumai, S. Horiuchi, A. Sawa, and T. Hasegawa, Field-Modulation Imaging of Ferroelectric Domains in Molecular Single-Crystal Films, *Phys. Rev. Appl.* **11**, 014046 (2019).
- [44] T. Hayashida, Y. Uemura, K. Kimura, S. Matsuoka, D. Morikawa, S. Hirose, K. Tsuda, T. Hasegawa, and T. Kimura, Visualization of ferroaxial domains in an order-disorder type ferroaxial crystal, *Nat. Commun.* **11**, 4582 (2020).
- [45] T. Ishibashi, Z. Kuang, S. Yufune, T. Kawata, M. Oda, T. Tani, Y. Iimura, K. Sato, Y. Konishi, K. Akahane, X. Zhao, and T. Hasegawa, Magneto-optical imaging using polarization modulation method, *J. Appl. Phys.* **100**, 093903 (2006).
- [46] P. J. Brown, J. B. Forsyth, and F. Tasset, A study of magnetoelectric domain formation in Cr_2O_3 , *J. Phys.: Condens. Matter* **10**, 663 (1998).

- [47] J. F. Dillon, H. Kamimura, and J. P. Remeika, Magneto-optical properties of ferromagnetic chromium trihalides, *J. Phys. Chem. Solids* **27**, 1531 (1966).
- [48] S. D. McClure, Comparison of the crystal fields and optical spectra of Cr_2O_3 and ruby, *J. Chem. Phys.* **38**, 2289 (1963).
- [49] K. A. Wickersheim, Optically observed exchange splittings in antiferromagnetic Cr_2O_3 , *J. Appl. Phys.* **34**, 1224 (1963).
- [50] E. Fischer, G. Gorodetsky, and S. Shtrikman, Critical behaviour of the magnetoelectric effect in Cr_2O_3 , *J. Phys. Colloq.* **32**, 650 (1971).
- [51] K. Momma and F. Izumi, Vesta3 for three-dimensional visualization of crystal, volumetric and morphology data, *J. Appl. Crystallogr.* **44**, 1272 (2011).
- [52] W. Kaiser, S. Sugano, and D. L. Wood, Splitting of the Emission Lines of Ruby by an External Electric Field, *Phys. Rev. Lett.* **6**, 605 (1961).